Bartlomiej MELKA[1], Jacek SMOLKA[1], Zbigniew BULIŃSKI[1], Arkadiusz RYFA[1], Janusz HETMANCZYK[2]

Institute of Thermal Technology, Silesian University of Technology (1), Department of Power Electronics, Electrical Drives and Robotics, Silesian University of Technology (2)

An experimental and numerical analysis of temperature and velocity field in PM BLDC motor

Abstract. In this paper, a validated numerical model was introduced to determine the temperature and velocity fields outside the electric motor. The analysed object was a brushless permanent magnet motor (PM BLDC) having a rated power of 431 W with neodymium permanent magnets located on the rotor. The temperature and velocity measurements were conducted using thermocouples and constant-temperature anemometers. The numerical model covered the investigated motor and the same unit working as a generator and the air volume around them in order to improve the heat dissipation conditions. The numerical results show a satisfactory agreement with the values obtained during the measurements.

Streszczenie. W pracy przedstawiono zwalidowany eksperymentalnie model numeryczny do wyznaczenia pola temperatury oraz prędkości na obudowie oraz wokół bezszczotkowego silnika elektrycznego małej mocy. Pomiary temperatury i prędkości przeprowadzono na stanowisku badawczym za pomocą termopar oraz anemometrów stałotemperaturowych i posłużyły one do walidacji modelu. Model numeryczny obejmował silnik wraz z obciążającą go prądnicą oraz bryłą powietrza wokół obu maszyn w celu dokładniejszego odwzorowania warunków wymiany ciepła. Wyniki otrzymane z modelu numerycznego wykazały satysfakcjonującą zgodność z wartościami otrzymanymi podczas pomiaru. Wyznaczania pola temperatury oraz prędkości na obudowie oraz wokół bezszczotkowego silnika elektrycznego małej mocy

Keywords: PM BLDC motor, CFD, heat transfer, thermal model
Słowa kluczowe: silnik PM BLDC, CDF, przepływ ciepła, model cieplny

Introduction

Nowadays, small and medium power Permanent Magnet Brushless Direct Current (PM BLDC) motors are widely applied as a source of drive systems. Many studies cover brushless motor applications for direct driving of vehicles [1][2]. The main advantages of PM BLDC are high efficiency, lack of mechanical commutation, which is replaced by electronic commutation, and high power density. A motor's durability and its lifetime are also dependent on the thermal load and mechanical material properties, especially in high speed PM BLDC motors [3]. The main disadvantage of PM BLDC motors is their high market price [4]. Thermal analysis of the device plays the key role in the motor design process [5]. The need for motor miniaturisation and the reduction of production materials makes it necessary to conduct a detailed thermal analysis.

A properly built mathematical model describing thermal phenomena could help to reduce the production costs,increase the device efficiency and extend the motor's lifetime [6]. To estimate the intensity of heat dissipation to the ambient air, the lumped model technique is often used by researchers during thermal analysis preparation [7][8][9]. However, lumped models do have restrictions considering their accuracy. The use of standard empirical equations, often implemented in the lumped models and describing heat transfer in the complex geometries, leads to some simplifications [10]. Hence, numerical field analyses are also used to complement this field of study [11]. Furthermore, the results of CFD simulations are quite often used as input data to lumped models [12].

Hence, the main aim of this study was to numerically determine the temperature and velocity fields on the external surface of a PM BLDC motor working on a dedicated test rig and in the surrounding air space. The developed thermal model has been validated by using temperature and velocity measurement points on the motor housing and around it.

Test rig

The test rig consisted of two identical PM BLDC motors. The first worked under rated parameters as a motor, while the second unit was used as a generator. Both machines were coupled by a universal bellow coupling. The motors were fastened to the base by an aluminium fixing and rubber separators. The base was used as the ground of the test rig. The separators provided sufficient thermal insulation between the aluminium fixing and the base.

The test rig was covered with an acrylic glass cover from the sides and the top. An 8 mm hole was drilled on the top cover wall to allow free outflow from the inside of the cover. The plexiglass cover allowed a natural air exchange from the bottom, between the volume inside the cover and the room's ambient air, because the cover protruded beyond the base. The cover was used in the test rig to limit the air fluctuations coming from the ambient room.

Nine thermocouples were attached to the motor housing. On each aluminium fixing one thermocouple was located. These eleven temperature probes, shown in Fig. 3, were used to validate the CFD model.

Additional measurements were used as the boundary conditions in the model. Three thermocouples measured the temperature on the generator housing. Four thermocouples were located above the motor at various heights relative to the rotational axis. Additionally, the temperature was measured on the inlet and outlet to the cover.

At the same height above the motor and generator, three constant temperature anemometers were used for the point velocity measurements. Studies referring to similar methods can be found in the literature [13][14]. Two of these anemometers were located above the motor and the third was set above the generator. The locations of these sensors are denoted by Roman numerals in Fig. 3.

Thermal and electric measurements were used to determine the losses in the motor. They were conducted for steady state for three loads, and reached respectively 33%, 58% and 80% of the rated load.

Temperature and velocity measurements were collected for 20 seconds for each steady state at given operating points. The average values of the parameters were consequently calculated. Apart from the main parts of the test rig, other components had to be applied as well, namely: power supply, electronic commutator, generated energy dissipation system, measurements record system. The heat dissipation system consisted of the springs which were connected to the generator and they dissipated the

generated electric power via heat transfer to the ambient air. This system was also supported by the cooling component supplied by an independent power source. The whole auxiliary system with electronic commutation was located beyond the test rig. The first five thermocouples located on the motor were of T type with uncertainty at a level of 0.5 K. The rest of the thermocouples used in the study were of J type and they had uncertainty at a level of 1.5 K. In the case of velocity measurements, statistical uncertainties were determined.

Losses in PM BLDC motor

The main losses in the PM BLDC motors are losses in the winding (also called copper losses) and losses in the magnetic circuit (iron losses). Other losses, such as mechanical losses, play a less important role. Moreover, additional losses in the regular velocity motor could be omitted because they are very small, and have hence been neglected in the analysed case. The sum of the mentioned losses can be written according to Eq. (1).

(1) $$\Delta P_{lossM} = P_{Cu} + P_{Fe} + P_{mec} + P_{ad}$$

where: ΔP_{lossM} is the sum of all losses in the machine, P_{Cu} is the copper loss, P_{Fe} is the iron loss, P_{mec} is the mechanical losses and P_{ad} is the additional loss.
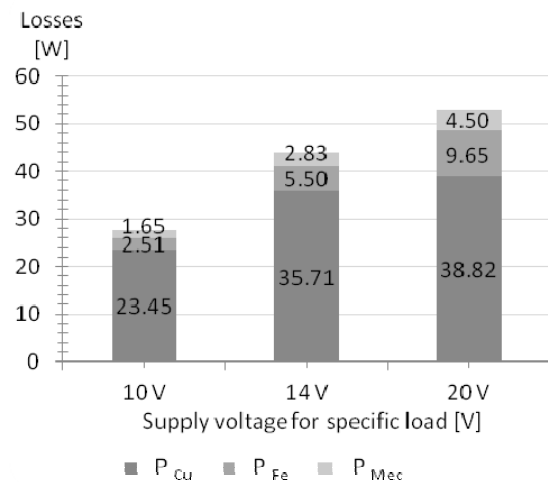

Figure 1 Loss values in the considered PM BLDC motor for the three voltage levels.

The copper losses result directly from the Joule heat generation caused by current flow through a conductor with the specific resistance. For all the studied operating points, the motor winding resistance can be expressed as a function of temperature. To find the proper winding temperature, an iterative method was implemented. In the first computation step the volume heat generation was applied to the numerical model - quantitatively equal to the losses arising from the device efficiency given by the producer. The currents in the specific phases were measured using a clamp meter. The sum of copper losses on the specific phases was used in the heat-flow model as a homogeneous volume heat generation. Winding resistance was calculated based on the average copper temperature taken from the numerical model. The copper losses, illustrated in Fig. 1, did not increase proportionally with the increasing load. Copper losses of 23.4 W were calculated for the load of 33%. Increasing the load by 25% resulted in a rise in copper loss of 12.3 W. Increasing the load by a further 22%, the copper losses grew by only 3 W.

Iron losses, also called the no-load loss, depend on induction and frequency (rotational speed of rotor). In the heat-flow model, the iron losses were also included in the

form of a homogeneous volume heat source. This heat source was applied in the same place where the magnetic circle was located. The iron losses depend on the frequency, which is connected with the rotational speed. The core losses of 2.5 W corresponded to the lowest tested load. For higher loads, iron losses were at levels of 5.5 and 9.7 W respectively. Fig. 1 shows the changes of these loads.

Mechanical losses, whose main source is friction in bearings, were determined by using an analytical method. The sum of the copper and iron losses from the motor and generator was subtracted from the measured input power of the system. It was assumed that mechanical losses were the same in each device because the machines were the same and worked with the same rotational velocities. Therefore, the obtained results were divided equally between the two machines. The mechanical losses were implemented in the numerical model as surface heat sources in the bearing. According to Fig. 1, the mechanical losses rise evenly with the increasing motor rotational velocity. For a rotational velocity of 1230 rpm and a supply voltage of 10 V, the mechanical losses were estimated as 1.65 W. At a higher rotational speed of 1944 rpm, the mechanical loss increased by 1.18 W. For the next load and speed of 2781 rpm, the loss increased by 1.67 W.

Additional losses can be represented by the air friction effect which in the type of motor (regular speed machine) analysed here could be neglected.

The internal structure of the generator was omitted in the model in order to reduce the computing time. Instead, the generator losses were defined by the inhomogeneous temperature profile on the external part of the housing. The temperature profile along the motor axis was estimated on the basis of the temperature measurements. The losses occurring in the electronic commutation, along the whole length of the input and output power cables, were not included in the numerical model because they were outside the computational domain as described in the previous chapter.

Numerical model

The numerical model including the motor and the air that surrounds both machines was built. The mesh consisted of almost 7 million elements. The governing equations on which the model was constructed included the mass, momentum and energy conservation equations [15]. The turbulence model used in the simulation was a standard k-ε model [15]. It is recommended to use the modified version of this model for the flow induced by a rotational environment such as in the case of the internal parts of a motor [16]. However, in an effort to reflect the phenomena on the external part of the motor housing in a proper way, it was implemented as a standard k-ε model. Radiation was simulated by using a discrete ordinates (DO) model [15][17]. In the model, higher pixelation was applied. The angle division was set to 4 for each octant of space, while the pixelation of the control angle was defined as 3.

The imaginary faces between the cover edges and the base of the test rig were modelled as the inlet boundary condition of the ambient pressure. The hole drilled in the top wall was included as a constant pressure outlet boundary condition. Because the model did not include the internal structure of the generator, the measured temperature profiles were defined on the external walls of the generator housing and aluminium fixing walls. In addition, the local heat transfer coefficients calculated from the empirical equation [18] were implemented as the boundary condition on the external domain boundaries, including the ambient temperature of the lab.

The model required a definition of the following air properties: density, specific heat, dynamic viscosity, and thermal conductivity as a function of the temperature. The thermal properties for the magnetic circuit and winding were treated as anisotropic values. Along the winding, the thermal conductivity was 167.3 W/(mK) and across the winding this parameter was 1.4 W/(mK). The thermal conductivity of the iron core was also adopted as 4.9 W/(mK) and 22.2 W/(mK) along and across the core, respectively. These data were assumed according to [19][20].

In the numerical model, on the contact surfaces between the air and coupling, the rotational speed was assumed based on the indications of an oscilloscope plugged into the commutator. Simulation of the shaft and magnets rotation was realised by setting the rotational speed on the interface between the air and rotor. The measured velocities implemented in the model were 1230 rpm, 1944 rpm and 2781 rpm for the considered cases with the increasing loads. Consequently, the rotational speed influenced the velocity field inside the motor.

Results and discussion

Table 1 presents the comparison of the experimentally obtained point temperatures and the temperatures calculated from the CFD model. The results are shown for three operating conditions. The locations of the temperature sensors listed in Table 1 are presented in Fig. 3.

Table 1. Comparison of experimental (Exp.) and calculated (CFD) temperatures in °C on and around the considered motor for three loads.

No.	Probe location	% of rated load						
		33 % for 10 V of supply voltage		58% for 14 V of supply voltage		80% for 20 V of supply voltage		Measurement uncertainty - type B
		Temperature, °C						
		Exp.	CFD	Exp.	CFD	Exp.	CFD	
1	Motor	48.5	49.3	59.5	60.9	66.3	66.0	0.5
2	Motor	48.7	49.9	59.8	61.8	66.8	67.3	0.5
3	Motor	47.7	48.1	58.1	58.9	64.9	64.1	0.5
4	Motor	49.0	49.3	60.0	60.9	66.9	66.0	0.5
5	Motor	48.1	48.6	58.9	59.8	65.8	65.1	0.5
6	Motor	48.3	49.7	59.4	61.5	66.4	66.9	1.5
7	Motor	48.4	49.3	59.5	60.9	66.4	66.0	1.5
8	Motor	48.3	49.7	59.2	61.4	66.2	66.8	1.5
9	Motor	47.2	48.0	57.4	58.8	64.1	64.0	1.5
10	Fixing	45.7	46.9	55.1	57.0	61.3	62.0	1.5
11	Fixing	46.8	47.9	56.8	58.7	62.4	63.4	1.5
12	Air	31.1	31.4	34.7	35.7	38.6	38.4	1.5
13	Air	31.1	31.5	34.8	36.6	38.7	39.8	1.5
14	Air	31.1	32.7	34.8	36.2	39.2	39.8	1.5
15	Air	31.3	32.7	35.2	36.8	39.1	39.3	1.5

Inaccuracy between the experiment and model results for the first five points did not exceed 2 K. The rest of the thermocouples used in the study were of J type. The maximal difference in that case was 2.2 K. The highest temperature, on the external housing wall, was in the region where the stator winding was located. This is obvious because the highest losses occur in that region. It can be seen that for all loads the temperature in the region of the front motor part, i.e. points #1, #2, #4, #6, #7, #8, is slightly higher than for the back part characterised by points #3, #5, #9. The probes #4, #8, #9, #10 are not presented in Fig. 3 because they are not visible from this perspective. However, the temperature on the housing surfaces is rather uniform. The highest difference between the temperatures measured on the motor housing was 2.8 K for the highest load. In the model, the highest temperature difference of 3.3 K appeared on the motor housing for the load of 80% of the rated load.

The model and measurement results in the form of the vertical component values of the velocity vector are shown in Figure 2. All the velocity probes were located 12.5 cm above the top walls of the motor and generator. The first two probes were installed above the motor #I, #II and the third one above the generator #III as shown in Fig. 3. All velocities were lower than 0.15 m/s for the 33% load. In this case, the CFD and measurement results reached the highest accuracy. For higher load, velocities from the first two probes exceeded values of 0.15 m/s in the CFD model, but the measured values were below this level. For the third probe, the results were the opposite. Moreover, the CFD values were within the measurement error value, except the last one. The velocity values from the measurements and CFD model for the highest load were greater than 0.15 m/s, except the last probe. Its value from the CFD model was also beyond the measurement error limit, although the first two were within this limit.
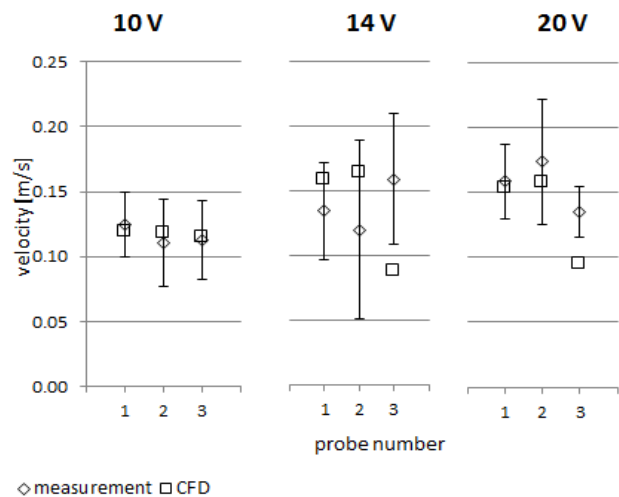

Figure 2 Vertical components of the velocity vectors in m/s at three locations above the motor for the three loading conditions.

Uncertainties of type A, which are the consequence of statistical analysis, are also included in this figure. The majority of the velocity values remain within the measurement error limits. One can see that, together with the increase of the load, the velocity above the coupled machines increases as well. This could be caused by the fact that at higher loads the quantity losses are also greater.

Consequently, higher heat generation and intensification of natural convection appears within the system, which directly affects the velocity rise above the components.

For higher loads, the generator housing temperature level started to significantly exceed the motor housing temperature. This could be caused by the fact that for the higher loads in the generator winding a higher current was flowing. This happened because the power dissipation system consisted of spring resistors having high inductance.

The temperature field around the motor demonstrates satisfactory agreement between the measurements and model results.
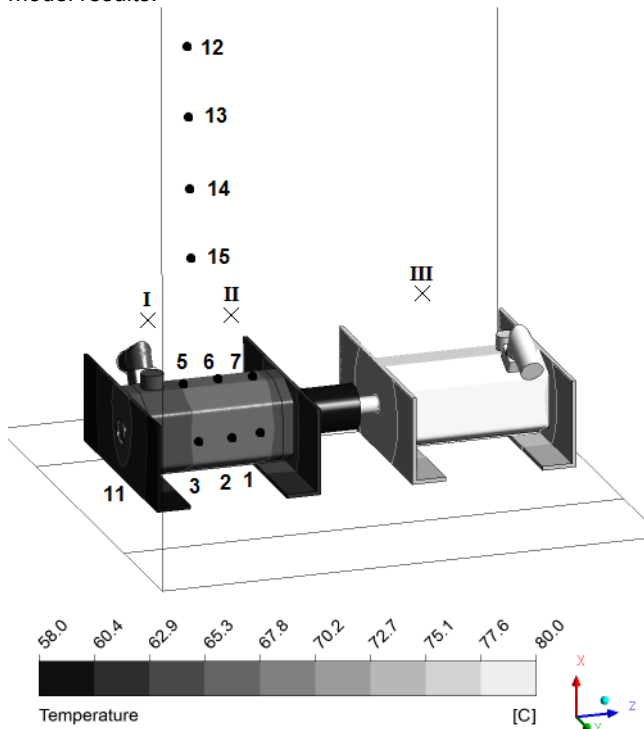

Figure 3 Temperature in °C on the external walls of the motor and generator for the highest tested load.

Conclusions

A test rig containing a PM BLDC motor was built for the purposes of this study. It was used to conduct temperature and velocity measurements on and around the motor. Subsequently, a CFD model reflecting the thermal motor behaviour on the test rig was prepared. Comparison between the results of the measurements and CFD showed a satisfactory accuracy.

Authors: Bartlomiej Melka M.Sc., Institute of Thermal Technology, Silesian University of Technology, Konarskiego 22, 44-100 Gliwice, E-mail: bartlomiej.melka@polsl.pl; Jacek Smolka Ph.D., D.Sc., Institute of Thermal Technology, Silesian University of Technology, Konarskiego 22, 44-100 Gliwice, E-mail: jacek.smolka@polsl.pl; Zbigniew Bulinski Ph.D., Institute of Thermal Technology, Silesian University of Technology, Konarskiego 22, 44-100 Gliwice, E-mail: zbigniew.bulinski@polsl.pl; Arkadiusz Ryfa Ph.D., Institute of Thermal Technology, Silesian University of Technology, Konarskiego 22, 44-100 Gliwice, E-mail: arkadiusz.ryfa@polsl.pl; Janusz Hetmanczyk Ph.D., Department of Power Electronics, Electrical Drives and Robotics, Silesian University of Technology, Krzywoustego 2, 44-100 Gliwice, E-mail: janusz.hetmanczyk@polsl

REFERENCES

[1] Luo F., Yeo H., Advanced PM brushless DC motor control and system for electric vehicles, *Industry Applications*, 2 (2000), 1336-1343
[2] Chau K., Chan C., Liu C., Overview of permanent-magnet brushless drives for electric and hybrid electric vehicles, *IEEE Transactions on Industrial Electronics*, 55 (2008), n. 6, 2246-2257
[3] Makieła D., Sensorless control of high-speed PM BLDC motor, *Proceedings of IEEE International Symposium on Industrial Electronics, Gdańsk*, (2011), 722-727
[4] Petrov I., Pyrhonen J., Performance of low-cost permanent magnet material in PM synchronous machines, *IEEE Transactions on Industrial Electronics*, 60 (2013), n. 6, 2131-2138
[5] Sebastian T., Temperature effects on torque production and efficiency of PM motors using NdFeB magnets, *IEEE Transactions on Industry Applications,* 31 (1995), n. 2, 353-357
[6] Boglietti A., Cavagnino A., Staton D., Shanel M., Mueller M., Mejuto C., Evolution and modern approaches for thermal analysis of electrical machines, *IEEE Transactions on Industrial Electronics*, 56 (2009), n. 3, 871-882
[7] Mellor P., Roberts D., Turner D., Lumped parameter thermal model for electrical machines of TEFC design, *Inst. Elect. Eng.*, 138 (1991), n. 5, 205–218
[8] Rostami N., Feyzi M.R., Pyrhonen J., Parviainen A., Niemela M, Lumped-parameter thermal model for axial flux permanent magnet machines, *IEEE Transactions on Magnetics*, 49 (2013), n. 3, 1178-1184
[9] Wallscheid O., Bocker J., Design and identification of a lumped-parameter thermal network for permanent magnet synchronous motors based on heat transfer theory and particle swarm optimisation, *Proceedings of ECCE-Europe - 17th European Conference, Geneva Switzerland,* (2015), 1-10
[10] Xu Z., Tighe C., Galea M., Hamiti T., Gerada C., Pickering S.J., Thermal design of a permanent magnetic motor for direct drive wheel actuator, *Electrical Machines, Proceedings of ICEM 2014 International Conference on, Berlin Germany,* 2186-2192
[11] Boglietti A., Cavagnino A., Lazzari M., Pastorelli M., A simplified thermal model for variable-speed self-cooled industrial induction motor, *IEEE Transactions on Industry Applications,* 39 (2003), n. 4, 945-952
[12] Staton D.A., So E., Determination of optimal thermal parameters for brushless permanent magnet motor design, *Proceedings of 33rd IAS Annual Meeting Industry Applications Conference*, (1998), 41-49
[13] Lundström H., Sandberg M., Mosfegh B., Temperature dependence of convective heat transfer from fine wires in air: A comprehensive experimental investigation with application to temperature compensation in hot-wire anemometry, *Experimental Thermal and Fluid Science*, 32 (2007), n. 2, 649-657
[14] Tewari S., Jaluria Y., Calibration of constant-temperature hot-wire anemometers for very low velocities in air, *Review of Scientific Instruments*, (1990), n. 61, 3834-3845
[15] Anderson J., *Computational fluid dynamics. The basics with applications*, McGraw-Hill, New York (1995)
[16] Saqr K., Aly H., Wahid M., Sies M., Numerical simulation of confined vortex flow using a modified k-epsilon turbulence model, *CFD Letters*, 1 (2009), n. 2, 87-94
[17] Thynell S., Discrete-ordinates method in radiative heat transfer, *International Journal of Engineering Science*, (1998), n. 36, 1651-1675
[18] Cengel Y.A., *Heat Transfer: A Practical Approach. 2nd ed.*, McGraw-Hill, New York (2002)
[19] Wrobel R., Mellor P., Holliday D., Thermal modelling of a segmented stator winding design, *IEEE Transactions on Industry Applications*, 47 (2011), n. 5, 2023-2030
[20] Wrobel R., Mellor P., A general cuboidal element for three-dimensional thermal modelling, *IEEE Transactions on Magnetics*, 46 (2010), n. 8, 3197-3200